Lattice-Boltzmann modelling of the quiet and unstable PRECCINSTA burner modes

Song Zhao, Karthik Bhairapurada, Muhammad Tayyab, Renaud Mercier, Pierre Boivin

Lattice-Boltzmann modelling of the quiet and unstable PRECCINSTA burner modes.

Song Zhao[1a], Karthik Bhairapurada[a], Muhammad Tayyab[a], Renaud Mercier[b], Pierre Boivin[a]

[a] *Aix Marseille Univ, CNRS, Centrale Marseille, M2P2, Marseille, France*
[b] *SAFRAN Tech, Digital Sciences & Technologies Department, Rue des Jeunes Bois, Châteaufort, 78114 Magny-Les-Hameaux, France*

Abstract

Recent studies have shown that Lattice-Boltzmann methods are indeed very promising in the field of reactive flows. More work is required, however, to demonstrate its ability to tackle complex reacting cases, as no study – to the authors' knowledge – involves simultaneously high Reynolds flows (for which the collision kernel needs specific care), complex geometries (for which models are required at the wall boundaries), and non-uniform grids (where non-conform meshes need to be addressed).

The present study intends to fill that gap, by investigating the well-known PRECCINSTA burner, including (i) characteristic boundary conditions, (ii) classical turbulent combustion modeling, (iii) multi-level grid refinements. Combining these elements, numerical simulations of the PRECCINSTA burner are carried out, both for the quiet ($\varphi = 0.83$) and unstable regimes ($\varphi = 0.7$). In both regimes, results are consistent with those obtained with classical (Navier-Stokes) solvers, but at a much lower cost. In particular,

[1] song.zhao@univ-amu.fr

it is the first time that successful prediction of thermoacoustic instabilities in a complex burner is shown in the framework of Lattice-Boltzmann methods.

Keywords: Lattice-Boltzmann methods; LBM; turbulent combustion; PRECCINSTA; TFLES; combustion instabilities

---

Introduction

Lattice-Boltzmann methods (LBM) are attracting more and more attention in the field of computational fluid dynamics, due to (i) the low arithmetic intensity of the nearest-neighbors lattice LBM [1] leading to very competitive CPU efficiency – including for reacting flows [2] – and (ii) its associated octree and cut-cell strategies, able to discretize rapidly very complex geometries, e.g. full-scale aircrafts [3]. Very recently, Bellotti et al. [4] proved rigorously LBM to be equivalent to a multi-step explicit macroscopic finite difference scheme on conserved moments, but LBM requires a shorter spatial stencil (at the cost of a higher number of variables).

Initially designed for isothermal flow with constant sound speed [5–8], adjustments for thermal and compressible flows were proposed in the past years [9–14] with undeniable success. The most recent applications of such models include simulations of supersonic cavities presented by Singh *et al.* [15], large eddy simulations of thermal impinging jets by Nguyen *et al.* [16], and of a 3D wing in transonic regime by Coratger *et al.* [17].

Realizing the advantages of such a framework, different groups have recently undertaken major steps towards Lattice-Boltzmann modelling of reacting flows [18–25], with a clear acceleration in recent years. Among the promising methods is the Hybrid compressible Lattice-Boltzmann method [21, 22],

which allows tackling flows with an arbitrary equation of state and transport models in a straightforward way.

Given (i) the excellent dissipation properties of LBM for acoustic propagation [26], including for hybrid methods [12, 13] for which vortical and acoustic mode propagations are convected by the LBM scheme [27–29] while species/entropy modes are convected with a specifically designed scheme [30, 31] ; and (ii) the success encountered in simulating burners with complex geometries [23, 25] for a reasonable cost, the next logical step is to investigate and develop LBM able to model thermo-acoustic instabilities.

This was performed for the first time last year, in a canonical narrow tube configuration [32], validating the thermoacoustic behavior of the hybrid method. In particular, the study validated the self-excitation of the flame in a quarter-wave unstable mode observed both experimentally [33, 34] and numerically [35, 36]. Comparisons were also performed with DNS predictions of Jiménez *et al.* [36].

The challenge is now to assess this hybrid LBM on a configuration close to aeronautical applications in terms of Reynolds number, Mach number but also geometry complexity. For this study, the PRECCINSTA (PREdiction and Control of Combustion INSTAbilities) burner is selected as (i) the experiment was specifically designed to be representative of an aeronautical injection system ; (ii) it has been widely characterized experimentally [37–40] ; (iii) it has been widely used in the literature to calibrate and validate the turbulent combustion numerical and modelling strategies both in stable and unstable regimes as recalled in the following.

Early Finite Volume LES studies were initiated by Lartigue et al. [40] who

performed the first non-reacting LES of the burner and identified the Precessing Vortex Core (PVC), a characteristic structure of such swirled flows governing flame stability. Several reacting computations have then been conducted on the PRECCINSTA burner to validate numerous turbulent combustion models, mainly on stable operating conditions. Presumed PDF modeling coupled with tabulated chemistry was assessed by Galpin et al. [41]. Later, an extension of tabulated chemistry was derived by Fiorina et al. [42] using a spatial filtering formalism to better cope with LES mathematical framework (F-TACLES model). After that, a first DNS (except for boundary layers) of the burner has been reached by Moureau et al. [43] using tabulated chemistry. In the same study, the authors used these reference results to improve the flamelet filtering concept to better account for subgrid-scale wrinkling (FLF-PDF model). A similar coupling between Filtered Density Function and low-dimensional manifolds (REDIM model) has also been validated on the PRECCINSTA burner by Wang et al. [44]. Later, the dynamic estimation of the subgrid-scale wrinkling function has also been validated a priori on the DNS database [43] by Veynante and Moureau [45]. PRECCINSTA was also used to benchmark combustion modeling approaches. See and Ihme [46] proposed a comparison of two tabulated chemistry approaches on the prediction for major species. Diffusion flamelets tabulation (FPV model) was compared to premixed flamelets tabulation (F-TACLES model) and sensible variations were found in the flame base region. After this comparison of chemistry modeling, the turbulent combustion closures have also been benchmarked by Wang et al. [47]. Both Dynamic Thickened Flame and Flame Surface Density models were considered to this end. Later in 2019, heat losses at

the walls of the burner were accounted for within the numerical modeling by Bénard et al. [48] who showed that the outer flame branch was in fact quenched by the cross-effect of heat losses and strain rate. Unstable operating conditions have also been investigated using LES. Among others, the work of Franzelli et al. [49] in 2012 showed a very good agreement with available measurements both on stable and unstable cases with the Thickened Flame Model. Later, Fredrich et al. [50] used a transported PDF approach to capture properly unstable operating points. To the authors' knowledge, the first reacting computation based on an LBM framework was performed recently by Hosseini et al. [25], also using a hybrid LBM approach. This study was however carried out in the low-Mach approximation, thus being incompatible with thermo-acoustic studies. Another important difference is the non-uniform discretization adopted here, allowing for mesh convergence study on complex geometry, and significantly reduced CPU costs.

The objective of this work is therefore to assess the ability of the hybrid compressible Lattice-Boltzmann method [17, 23] to tackle this aeronautical-like turbulent premixed flame in both thermoacoustically stable and unstable regimes. The first Section of this article will describe the numerical strategy including the turbulent combustion modeling choices. Then, the second Section will analyze the simulation of the stable operating condition of the burner. A third section will detail the results obtained using the same numerical strategy under unstable operating conditions.

1. Lattice-Boltzmann method for the PRECCINSTA burner

1.1. Governing equations

In the present work, the classical fully compressible Navier-Stokes (NS) equations for reactive flows are considered. Conservation laws of mass, momentum, total energy and species mass fractions read

$$\frac{\partial \rho}{\partial t} + \frac{\partial \rho u_\beta}{\partial x_\beta} = 0 \tag{1a}$$

$$\frac{\partial \rho u_\alpha}{\partial t} + \frac{\partial \rho u_\alpha u_\beta}{\partial x_\beta} = -\frac{\partial p}{\partial x_\alpha} + \frac{\partial \tau_{\alpha\beta}}{\partial x_\beta} \tag{1b}$$

$$\frac{\partial \rho E}{\partial t} + \frac{\partial \rho u_\beta E}{\partial x_\beta} = -\frac{\partial p u_\beta}{\partial x_\beta} + \frac{\partial \tau_{\alpha\beta} u_\alpha}{\partial x_\beta} - \frac{\partial q_\beta}{\partial x_\beta} \tag{1c}$$

$$\frac{\partial \rho Y_k}{\partial t} + \frac{\partial \rho u_\beta Y_k}{\partial x_\beta} = \frac{\partial J_\beta^k}{\partial x_\beta} + \dot{\omega}_k \tag{1d}$$

where ρ is the density, u_α the α-th component of the velocity, E the total energy (sum of internal e and kinetic energies κ)

$$E \equiv e + \kappa = h - \frac{p}{\rho} + \frac{1}{2}u^2 = \sum_{k=1}^{\mathrm{N_{sp}}} (Y_k h_k) - \frac{p}{\rho} + \frac{1}{2}u^2 \tag{2}$$

where h_k is the enthalpy of species k

$$h_k \equiv \int_{T_0}^{T} c_{p,k}(\theta) d\theta + \Delta^0 h_k \tag{3}$$

with $c_{p,k}$ is the constant pressure heat capacity of species k and $\Delta^0 h_k$ the formation enthalpy.

The species and thermal diffusion terms (J_β^k, q_β, respectively), viscous tensor $\tau_{\alpha\beta}$ and chemical source terms $\dot{\omega}_k$ require modelling, as defined hereafter.

1.2. Models

In practice, the governing equations are solved under their filtered form, with all closure terms provided in Appendix A. The closure models used are summarized below.

Equation of state. The ideal gas Equation of State (EOS) is employed hereafter. Internal energy/enthalpy is linked to the temperature T and species fractions through the classical NASA polynomials [51].

Transport model. Thermal and species properties are obtained assuming constant Schmidt (for each species) and Prandtl numbers, from a temperature-defined viscosity: $\mu = \mu_0(T/T_0)^{0.7}$. Their turbulent counterparts are obtained assuming constant turbulent Schmidt and Prandtl numbers $\mathrm{Pr_t} = \mathrm{Sc_t} = 0.7$.

Chemical source term. Here, the methane/air chemical mechanism proposed by Franzelli [52] is used, consisting of 2 global reactions among 6 species (CH_4, O_2, CO_2, H_2O, CO, N_2). The chemical source term is integrated explicitly under the exponential form, as shown in [53].

Turbulent model. The turbulent viscosity ν_t is obtained via the Vremann model [54], as described, e.g. in [17].

Turbulent combustion model. The classical thickened flame model [55] is used in its most recent version [56]. The objective of the model is to thicken the flame (detected by sensor $\mathcal{S}$) according to the grid resolution while preserving its velocity by multiplying the diffusion term and dividing the chemical source term by $\mathcal{F}$. The subgrid wrinkling effect is accounted for via an efficiency

function Ξ [57, 58], in its form proposed by Rochette et al. [59]. Further details are available in Appendix A.

1.3. Hybrid compressible Lattice-Boltzmann method for reactive flows

The filtered NS equations (A.1) are resolved using the hybrid compressible Lattice-Boltzmann method [17]. Flow fields (density, velocity) are calculated using the density-based unified hybrid LBM framework proposed for compressible flows [13], using a D3Q19 lattice.

In this model, the energy and species conservation are resolved in a Finite Difference (FD)/Finite Volume (FV) like manner. Thermal and species diffusion are discretized with second-order centered numerical schemes [21, 23].

At the algorithm center lies the convective operators. Convective terms in energy and species transport equations are evaluated using the LBM populations to achieve consistency between the LBM and FD/FV methods [30, 60]. The energy flux is discretized with a newly designed pseudo Double-Distribution-Function (pseudo-DDF) method detailed in Appendix B. The species flux is resolved using the monotone numerical scheme proposed in [30, 61] specially designed for mass fraction transport,

$$\nabla \cdot (\overline{\rho}\tilde{\boldsymbol{u}}\tilde{Y}_k) \equiv -\sum_i \Delta m_i \begin{cases} \tilde{Y}_k(\boldsymbol{x},t) & \text{if } \Delta m_i \leq 0 \\ \tilde{Y}_k(\boldsymbol{x}+\boldsymbol{c_i}\Delta t,t) & \text{otherwise.} \end{cases} \tag{4}$$

with

$$\Delta m_i \equiv f_{\bar{i}}(\boldsymbol{x}+\boldsymbol{c_i}\Delta t) - f_i(\boldsymbol{x}) \tag{5}$$

where $\bar{i}$ represents the lattice in the opposite direction of i. This numerical scheme constructs the species flux according to the difference of the probability distribution function (PDF) of this specie between neighbor lattices, an

approach more physical than classical methods [61]. The basic idea of this method is to construct the species flux based on the information embedded in the distribution functions. From a certain point of view, the resolved species field follows the Boltzmann equation instead of the Navier-Stokes equation, which is more fundamental and physical in a Lattice-Boltzmann framework.

1.4. Numerical set-up

Large-eddy simulations of the PRECCINSTA burner are conducted in the following Sections to assess the performance of the hybrid LBM solver. All simulations are carried out in the ProLB solver.

Simulation domain and meshes. The burner simulation domain is represented in Fig. 1, with a large downstream plenum to reduce acoustic re-

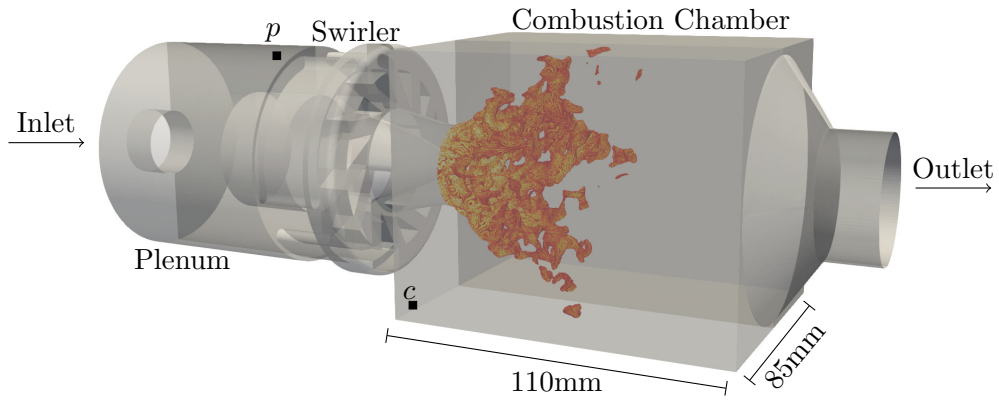

Figure 1: Global view of the PRECCINSTA setup along with the indication of the plenum (p) and chamber (c) probe locations.

flections from the burner outlet [40], visible e.g. in Fig. 2. Three meshes (M_0, M_1, M_2) are tested to study the convergence of the simulation as shown in Tab. 1. The mesh topology is presented in Fig. 2. Configurations M_0

and M_1 include five levels of mesh refinements: two in the combustor region (represented in Fig. 2.b), and another three in the outlet plenum (Fig. 2.a). The outlet plenum is the coarsest region, while the flame region is the finest, in a "V" shape characteristic of the swirl flame. The finest mesh M_2 is obtained from M_1 by adding a V-shaped finer sub-region (thus resulting in 6 mesh levels) while keeping the grid constant everywhere else. At each mesh transition, the grid size is doubled/halved, and so is the time step. The finest region of M_2 corresponds to $\Delta x = 0.15$mm. The total number of points, minimum grid size, and the corresponding numbers of points in flame thickness are reported in Tab. 1.

Table 1: Mesh configurations

	M_0	M_1	M_2
No. of pts.	2.4M	19.9M	81.2M
Minimum Δx	0.6 mm	0.3 mm	0.15 mm
Pts. in thickened δ_T^L	6	6	6

Boundary conditions. Boundary conditions are prescribed as follows: i) the inlet of the burner is set a non-reflecting inlet characteristic boundary condition [62], ii) the outlet is far-field pressure non-reflecting characteristic condition [63] and iii) walls are modeled as non-slip adiabatic walls.

Calculation initialization. The initialization is trivial for the M_0 mesh:

- uniform (atmospheric) pressure,
- uniform velocity (inlet velocity $u = 24$m/s),
- fresh gases at 300K until the swirler exit (i.e. for $x < 0$),

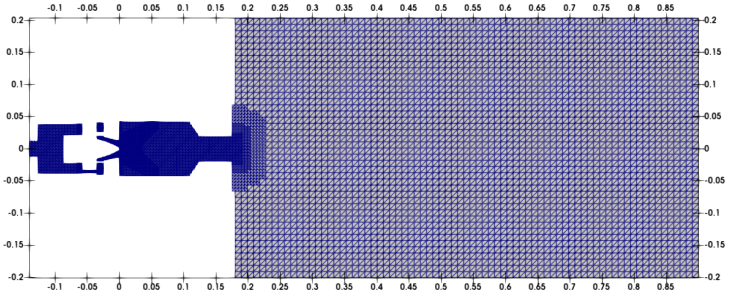

(a) Global topology

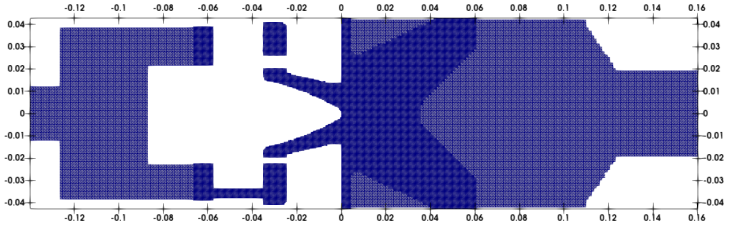

(b) Refinement near flame region

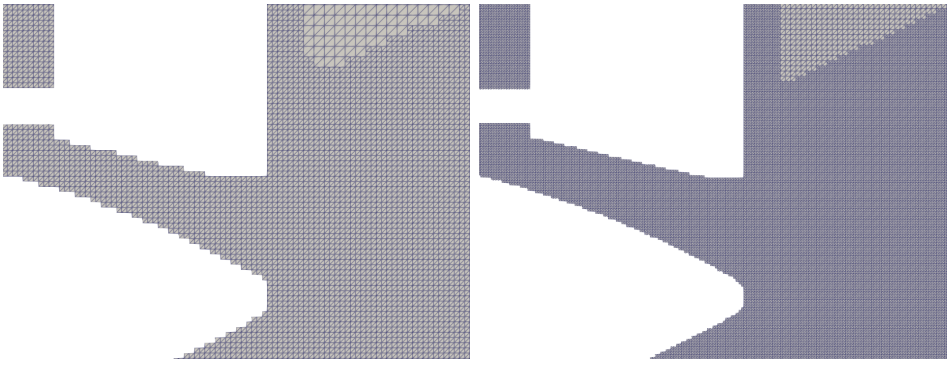

(c) Zoomed view near burner injector. Left M_0, right M_1.

Figure 2: Mesh refinement strategy represented along the axis cut plane.

- burnt gases for $x > 0$, at the adiabatic temperature.

In other words, no cold flow simulation is required (e.g. setting $\dot{\omega}_k = 0$), nor on-the-fly parameter change. After M_0 mesh simulation, M_n calculations are initialized through interpolation of M_{n-1} results. They are then carried out for $7t_c$, for stabilization, and again for $18t_c$, for statistics. Here, the characteristic convective time $t_c \approx 2\,\text{ms}$ is defined as a ratio of the flame length and bulk inlet velocity. The flame parameters of the investigated cases are given in Tab. 2.

Case	ϕ	T_{ad} (K)	δ_T^L (m)	$\mathcal{F}$	Inlet velocity (m/s)	P_{th} (kW)
Quiet	0.83	2058	0.41×10^{-3}	5	24.0	30
Unstable	0.7	1847	0.55×10^{-3}	3.5	24.0	25

Table 2: Simulation parameters for the quiet and unstable modes.

2. Large eddy simulation of the quiet mode

2.1. Qualitative agreement

Instantaneous axial cut-plane fields from the simulation M_2 are shown in Fig. 3. The flow and scalar fields are well recovered as well as the pressure drop across the swirler. The Q-criterion fields in Fig. 3(a) indicate the main vortex has been successfully generated by the swirl injector. A 3D volume view rendered by the heat-release rate is provided in Fig. 3(b). One can see that the M-shape flame is curved by the flow field quite significantly in the Heat Release Rate (HRR) fields (Fig. 3(d)), as well as the capturing of the unburnt pockets. Other configurations achieve similar global flow topology, although the M_1, M_0 simulations capture much less small-scale details.

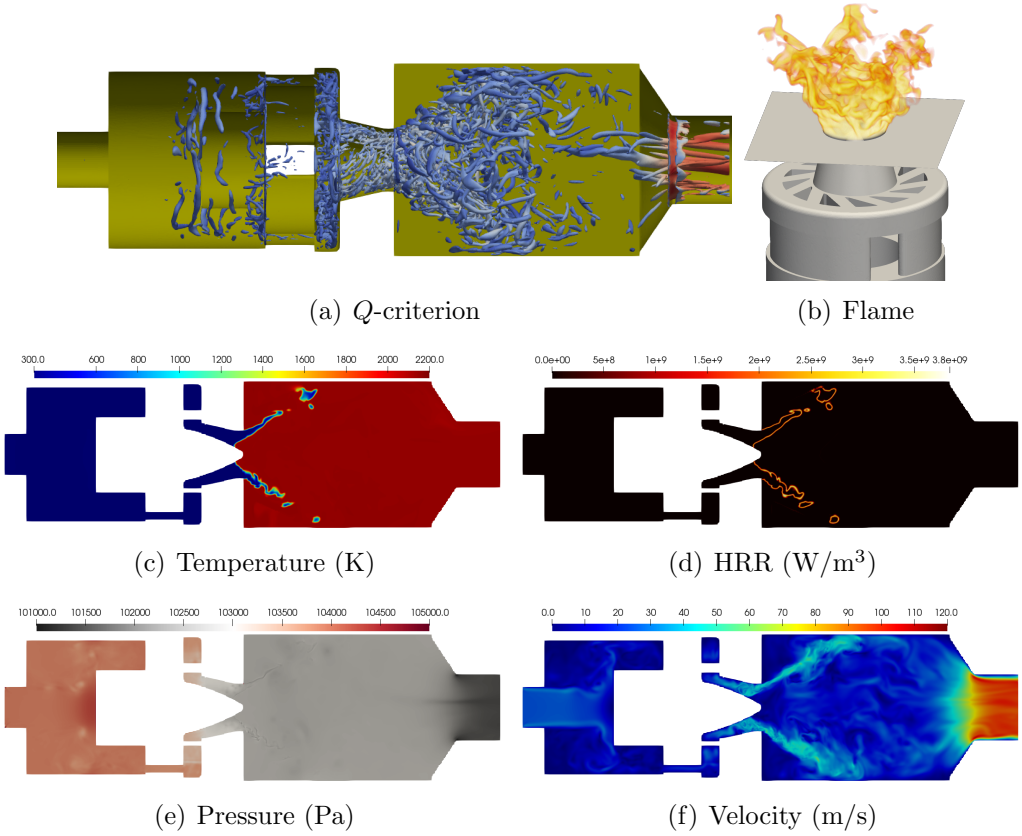

(a) Q-criterion (b) Flame

(c) Temperature (K) (d) HRR (W/m^3)

(e) Pressure (Pa) (f) Velocity (m/s)

Figure 3: Instantaneous flow fields.

2.2. Statistics on the cut-planes

The statistical results are considered on the cut-planes orthogonal to the burner axis in the combustion chamber. Quantities at cut-planes 6, 10, 15, 20, 30, and 40 mm from the injector exit are averaged azimuthally and presented with respect to the distance to the center in Fig. 4. These statistics are performed as temporal averages over at least two flow-through times. Experimental measurements are shown with black symbols when available. A reference simulation performed on a 2.4×10^6 nodes unstructured mesh ($\Delta_x = 0.6$ mm) by Moureau et al. [43] with YALES2 solver using a tabulated chemistry approach is also provided. The average curves from the left column show a good agreement with the experimental/reference data starting from the coarsest grid M_0. Note that the temperature behavior in the Outer Recirculation Zone (ORZ) is not well captured for all the configurations (M_0, M_1, M_2), because heat losses are neglected here [48]. The M_1 and M_2 configuration correctly predicts the temperature, velocity and major species in the Central Recirculation Zone (CRZ) as well as the flame front. However, M_0 configuration underestimates these quantities in the CRZ due to the loss of information given the large grid size. This is more evident through RMS values. Although the results are not so good for RMS profiles, the mean profiles show fairly good agreement with the experimental data. The M_2 simulation is slightly better than M_1 in RMS reproduction and almost the same for the mean profiles. Hence, the difference of results between the two grid sizes is marginal. Furthermore, it is clear from the profiles presented in Fig. 4 that reasonable grid convergence is achieved. It is observed that the coarse grid (M_0) produces the largest error compared to finer grid

sizes, whereas, M_1 grid captures sufficient information to produce comparable results to that of the experiments. Finally, M_2 results are slightly better as it captures smaller structures. In conclusion, this grid size is not necessarily required in order to achieve good agreement with the experimental data. The remainder of the study will hence focus on the M_1 discretization only.

3. Large eddy simulation of the unstable mode

Having recognized the capacity of LBM to perform studies on thermoacoustic instabilities in [32], we now extend it to the PRECCINSTA combustor. At the operating conditions $\phi = 0.7$ and $P_{th} = 25$kW, the combustor was shown to exhibit self-excited thermoacoustic instabilities [37, 64, 65] which is characterized by the pulsations of the flame up and down the stream in the combustion chamber. Considering the above operating conditions, and using the same characteristic boundary conditions, thickening model and mesh M_1 as in the quiet flame case, let us now study the pressure history at the two probes identified in Fig. 1.

The pressure drop (difference of pressure between plenum probe P_p and combustion chamber probe P_c) is plotted for both quiet and unstable modes in the Fig. 5. The mean pressure drop (ΔP) for both quiet and pulsating cases is around 1500 - 1800 Pa [64], but the maximum pressure drop for the pulsating case is much higher and the minimum reaches negative values every oscillation cycle. This certainly can be seen as one of the predictors for the onset of instability in this configuration.

The fluctuations of pressure signals in the plenum and combustion chamber are plotted in Fig. 6. As in the experiment [37], it can be seen that the

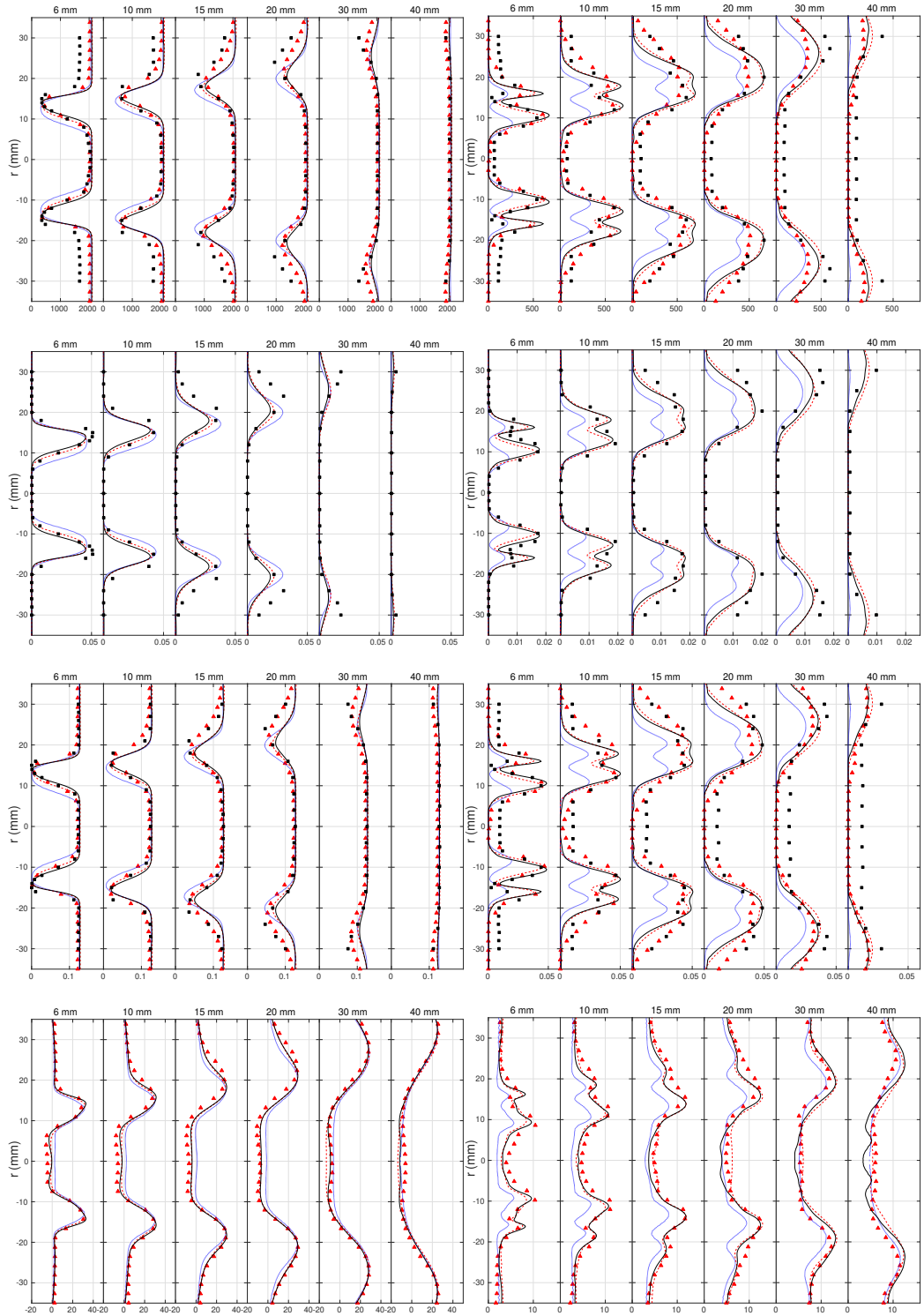

Figure 4: Quiet (or Stable) operating point ($\phi = 0.83$). Average (left column) and RMS (right column) values at cut planes vertical to the burner axis in the combustion chamber. Temperature (K) , CH_4, CO_2, Axial velocity (m/s) (from top to bottom). Black solid squares (experimental), red solid triangles (YALES2 M_0 reference), blue dotted line (M_0), red dashed line (M_1) and black solid line (M_2)

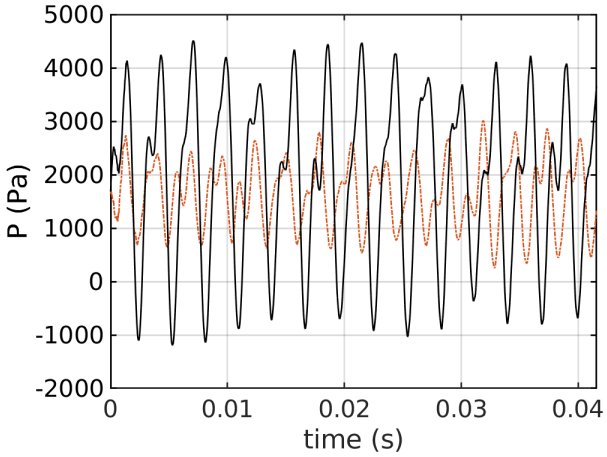

Figure 5: Pressure drop ΔP between the inlet plenum and the combustion chamber. Unstable (or pulsating) flame $\phi = 0.7$ (black solid line) and Stable (or quiet) flame $\phi = 0.83$ (orange dashed line)

trace of plenum pressure fluctuation (black) P_p is smoother than the combustion chamber P_c and that it lags behind the combustion chamber (blue). The power spectral density (PSD) of the plenum and chamber pressure fluctuation signals are plotted in the Fig. 6, and as observed the peak of the self-excited frequency obtained corresponds to 340 Hz and its harmonic can also be seen at around 680 Hz. It is also surprising to note that the power of the main frequency is slightly greater in the plenum whereas the harmonic seems to be stronger in the combustion chamber.

The time-averaged mean and RMS profiles of temperature and CO_2 mass fractions for the pulsating case are shown in Fig. 7. The match is reasonable for the mean profiles except for the already above-mentioned over-prediction on the ORZ due to adiabatic walls. The RMS profiles of temperature and CO_2 mass fraction clearly show the pulsations on the CRZ, but they are slightly under-predicted. These fluctuations of temperature and CO_2 mass

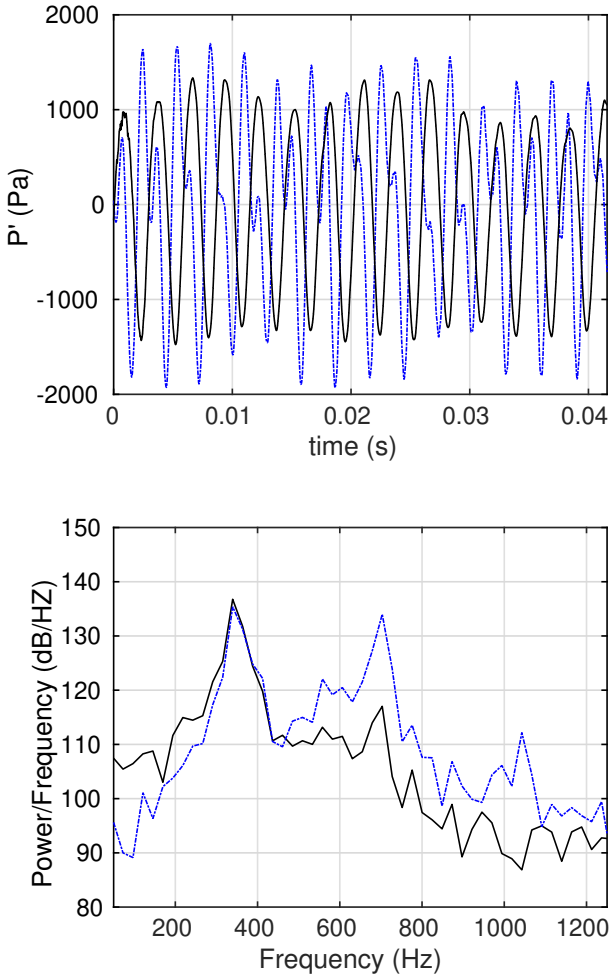

Figure 6: Unstable (or pulsating) ($\phi = 0.7$). Dynamic fluctuations of pressure in the plenum (solid in black) and chamber (dot-dash in blue) and their respective power spectral density (PSD) signals.

fraction can also be seen as a clear illustration of the difference between the quiet and pulsating cases.

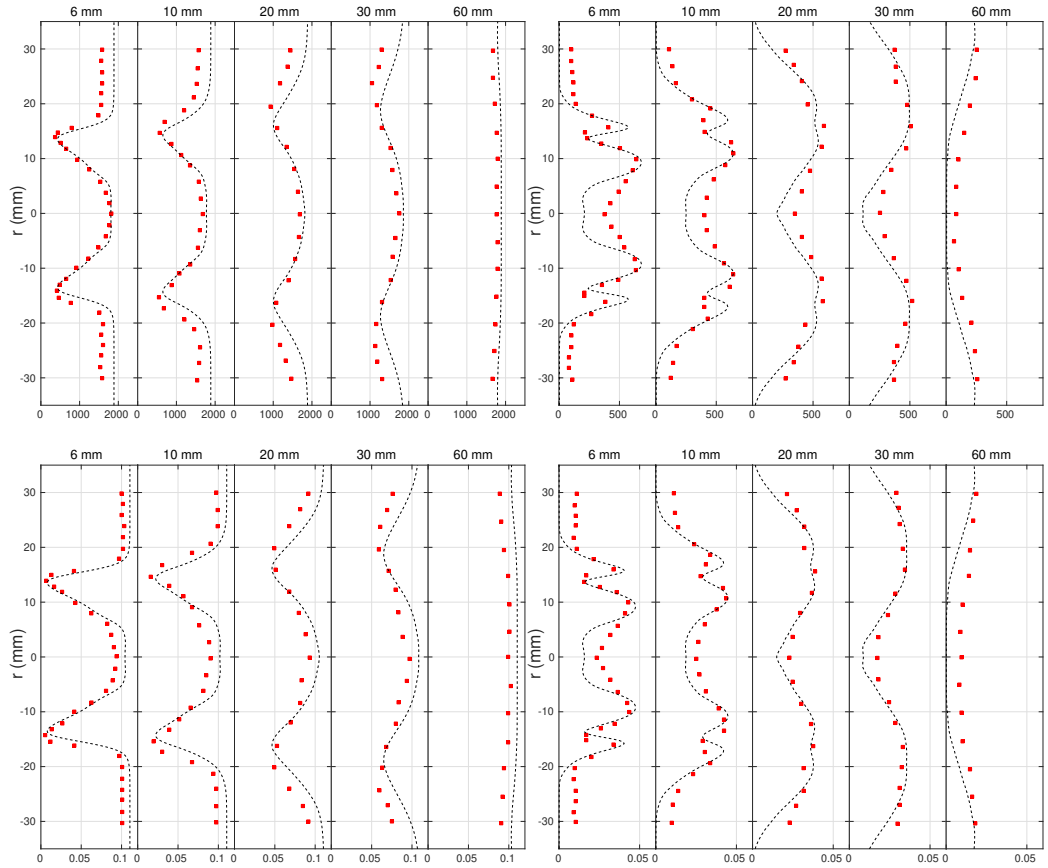

Figure 7: Unstable (or pulsating) ($\phi = 0.7$). Average (left column) and RMS (right column) values at cut planes vertical to the burner axis in the combustion chamber. Temperature (K) and CO_2 (from top to bottom). Red solid squares (experimental) and black dashed line (M_1)

Finally, Fig. 8 depicts the temporal fluctuations of total heat release rate and pressure in the combustion chamber P_c, showing that they are in phase. This indicates that the instability is fed by flame/acoustics coupling [37, 49, 65]. It should also be noted that these modes are also observed in the stable case, but their amplitudes are quite small.

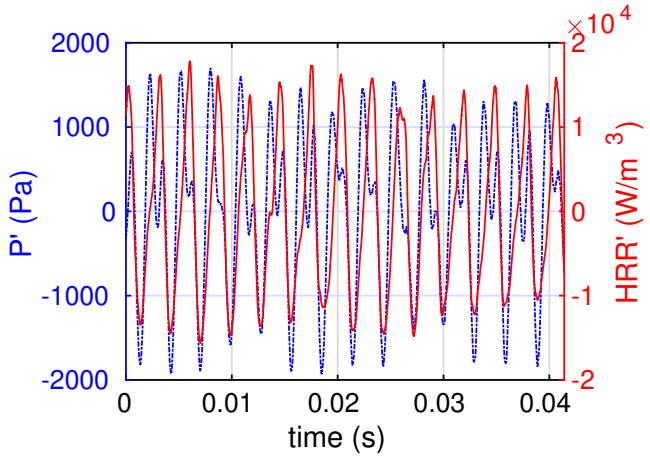

Figure 8: "In-phase" relationship between pressure fluctuations in the chamber (dot-dash blue line) and the total heat release fluctuations (solid red line) ($\phi = 0.7$)

Considering that the pressure drop is almost in phase with the plenum pressure fluctuations P_p, we plot the cycle of self-sustained oscillations as a function of plenum pressure fluctuations alongside the total HRR fluctuations in the Fig. 9. The eight phase angles are chosen approximately in accordance with Meier's experiments [37], only four of them are depicted here for clarity. The plenum pressure is minimum at phase Ph1, but since the heat release rate and chamber pressure fluctuations lead, they are growing rapidly. The combustion chamber pressure and the combustion intensity reach their maximum just after Ph3. This maximal chamber pressure forces the flame back upstream and the flame starts to disintegrate. The plenum pressure is maximum at phase Ph5, and since the drop of fluctuations is faster than their growth, the flame has already disintegrated quite a lot and moved back upstream. After this, the plenum pressure starts dropping rapidly and at phase Ph7, the combustion intensity reaches its minimum. The significant positive pressure drop between the plenum and chamber starts to force the

flame downstream, re-initiating the cycle again.

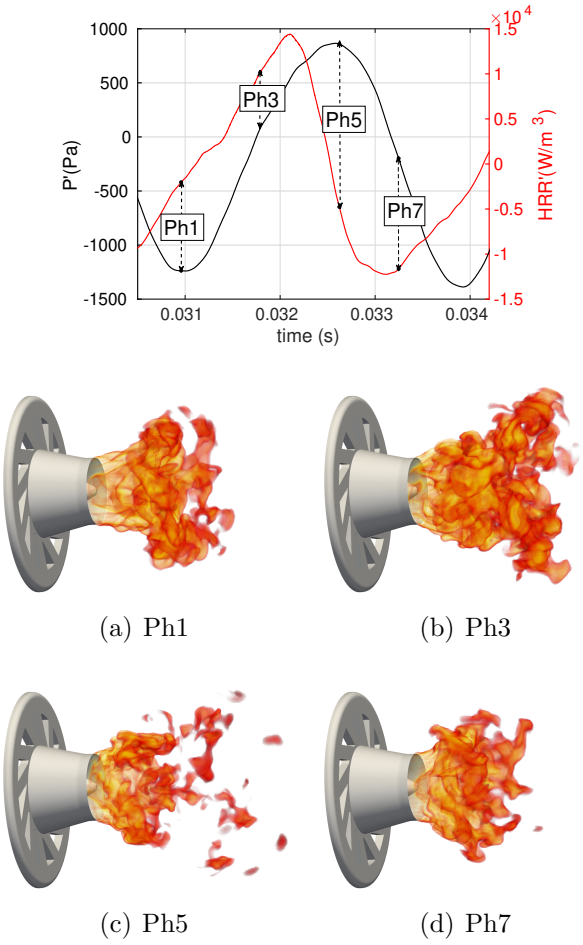

(a) Ph1 (b) Ph3

(c) Ph5 (d) Ph7

Figure 9: Illustration of instantaneous phase-locked isocontours of HRR with the temporal fluctuations of plenum pressure (black) and total HRR (red)

4. Concluding remarks and perspectives

We have presented a detailed numerical study of both quiet and unstable modes of the PRECCINSTA burner for the first time using a Lattice-Boltzmann solver. The study confirms that the Lattice-Boltzmann methods

are highly promising for the simulation of reacting flows in complex geometries, including the prediction of thermoacoustic instabilities.

Results are found to be comparable with those obtained with Navier-Stokes solvers and converge for a reasonably coarse mesh in the stable configuration (20M grid points) – at least for mean and RMS quantities. The unquiet configuration is also quite accurately recovered, given this study is the first of its kind. To improve predictions, we believe it is necessary to improve the turbulent combustion model (using, e.g., more advanced approximations for the efficiency exponent or a PDF turbulent model), use a more detailed kinetic description, and carefully take into account heat losses. This will be the focus of future studies.

On a concluding note, the method is also highly efficient, with numerical costs on the order of 5 µs of CPU time per iteration per grid point (reduced computation cost, RCT), excellent by the standards of reactive simulations (see, e.g. [66]). Translating to a perhaps more visual figure, this corresponds to about 450 CPU hours per convective time t_c for M_1 calculations, or less than 12000 CPU hours for a full M_1 run (including the initial M_0 run).

There are still several areas where improvements are needed. Firstly, we treat the temperature boundary conditions on solid walls as adiabatic, which can lead to inaccuracies in the temperature field near the wall. To address this issue, we will incorporate wall temperature/heat flux measurements into our simulations to ensure greater accuracy. Secondly, the current study uses the two-step BFER chemistry mechanism, but we believe that more detailed chemistry mechanisms should lead to greater accuracy in our simulations. Specifically, the 17 species reduced chemistry [67] used in the

reference YALES2 simulations will be tested, which may help capture more inner flame structures currently lacking in our simulations, especially in the M_0 simulation, regarding the low RMS values in M_0 simulations near the flame region. Finally, the impact of flame turbulence models on flame dynamics will be further investigated, especially in unstable cases. As discussed in [65], the evaluation procedure of the exponent parameter for the sub-grid wrinkling factor in the TFLES framework influences the flame-acoustic interactions. Exploring this issue under the hybrid-LBM framework may lead to a better understanding of how different flame turbulence model parameters can impact flame dynamics.

5. Acknowlegments

Dr. Vincent Moureau is gratefully acknowledged for providing the fluid computational domain of the PRECCINSTA Burner as well as simulation data from YALES2 solver simulations. Dr. Romain Pain and Mr. Julien Leparoux are also warmly thanked for fruitful discussions. Centre de Calcul Intensif d'Aix-Marseille and GENCI (Grant A0112B11951) are acknowledged for granting access to their high-performance computing resources. This research was supported by the MALBEC ANR project ANR-20-CE05-0009.

References

[1] J. Latt, C. Coreixas, J. Beny, Cross-platform programming model for many-core lattice boltzmann simulations, Plos one 16 (2021) e0250306.

[2] P. Boivin, M. Tayyab, S. Zhao, Benchmarking a lattice-boltzmann solver for reactive flows: Is the method worth the effort for combustion?, Phys. Fluids 33 (2021) 071703.

[3] M. R. Khorrami, E. Fares, Simulation-based airframe noise prediction of a full-scale, full aircraft, in: 22nd AIAA/CEAS aeroacoustics conference, 2016, p. 2706.

[4] T. Bellotti, Rigorous derivation of the macroscopic equations for the lattice boltzmann method via the corresponding finite difference scheme, arXiv preprint arXiv:2205.02505 (2022).

[5] S. Succi, R. Benzi, F. Higuera, The lattice boltzmann equation: a new tool for computational fluid-dynamics, Phys. D: Nonlinear Phenom. 47 (1991) 219–230.

[6] Y.-H. Qian, D. d'Humières, P. Lallemand, Lattice bgk models for navier-stokes equation, Europhys. Lett. 17 (1992) 479.

[7] S. Chen, G. D. Doolen, Lattice boltzmann method for fluid flows, Annu. Rev. Fluid Mech. 30 (1998) 329–364.

[8] T. Krüger, H. Kusumaatmaja, A. Kuzmin, O. Shardt, G. Silva, E. M. Viggen, The lattice boltzmann method, Springer International Publishing 10 (2017) 4–15.

[9] Y. Feng, P. Sagaut, W. Tao, A three dimensional lattice model for thermal compressible flow on standard lattices, J. Comput. Phys. 303 (2015) 514–529.

[10] Y. Feng, P. Boivin, J. Jacob, P. Sagaut, Hybrid recursive regularized thermal lattice boltzmann model for high subsonic compressible flows, J. Comput. Phys. 394 (2019) 82–99.

[11] J. Latt, C. Coreixas, J. Beny, A. Parmigiani, Efficient supersonic flow simulations using lattice boltzmann methods based on numerical equilibria, Philos. Trans. R. Soc. A 378 (2020) 20190559.

[12] G. Farag, S. Zhao, T. Coratger, P. Boivin, G. Chiavassa, P. Sagaut, A pressure-based regularized lattice-boltzmann method for the simulation of compressible flows, Phys. Fluids 32 (2020) 066106.

[13] G. Farag, T. Coratger, G. Wissocq, S. Zhao, P. Boivin, P. Sagaut, A unified hybrid lattice-boltzmann method for compressible flows: Bridging between pressure-based and density-based methods, Phys. Fluids 33 (2021) 086101.

[14] M. H. Saadat, S. A. Hosseini, B. Dorschner, I. Karlin, Extended lattice boltzmann model for gas dynamics, Phys. Fluids 33 (2021) 046104.

[15] D. Singh, A. F. Ribeiro, B. Konig, E. Fares, Lattice boltzmann simulations of a supersonic cavity, in: 35th AIAA Applied Aerodynamics Conference, 2017, p. 4461.

[16] M. Nguyen, J. Boussuge, P. Sagaut, J. Larroya-Huguet, Large eddy simulation of a thermal impinging jet using the lattice boltzmann method, Phys. Fluids 34 (2022) 055115.

[17] T. Coratger, G. Farag, S. Zhao, P. Boivin, P. Sagaut, Large-eddy lattice-boltzmann modeling of transonic flows, Phys. Fluids 33 (2021) 115112.

[18] K. Yamamoto, X. He, G. D. Doolen, Combustion simulation using the lattice boltzmann method, JSME International Journal Series B Fluids and Thermal Engineering 47 (2004) 403–409.

[19] E. Chiavazzo, I. V. Karlin, A. N. Gorban, K. Boulouchos, Combustion simulation via lattice boltzmann and reduced chemical kinetics, J. Stat. Mech.: Theory Exp. 2009 (2009) P06013.

[20] A. Xu, C. Lin, G. Zhang, Y. Li, Multiple-relaxation-time lattice boltzmann kinetic model for combustion, Phys. Rev. E 91 (2015) 043306.

[21] M. Tayyab, S. Zhao, Y. Feng, P. Boivin, Hybrid regularized lattice-boltzmann modelling of premixed and non-premixed combustion processes, Combust. Flame 211 (2020) 173–184.

[22] S. A. Hosseini, A. Eshghinejadfard, N. Darabiha, D. Thévenin, Weakly compressible lattice boltzmann simulations of reacting flows with detailed thermo-chemical models, Comput. Math. with Appl 79 (2020) 141–158.

[23] M. Tayyab, S. Zhao, P. Boivin, Lattice-boltzmann modeling of a turbulent bluff-body stabilized flame, Phys. Fluids 33 (2021) 031701.

[24] N. Sawant, B. Dorschner, I. V. Karlin, Consistent lattice boltzmann model for reactive mixtures, J. Fluid Mech. 941 (2022).

[25] S. A. Hosseini, N. Darabiha, D. Thévenin, Low mach number lattice boltzmann model for turbulent combustion: flow in confined geometries, Proc. Combust. Inst. (2022).

[26] S. Marié, D. Ricot, P. Sagaut, Comparison between lattice boltzmann method and navier–stokes high order schemes for computational aeroacoustics, J. Comput. Phys. 228 (2009) 1056–1070.

[27] G. Wissocq, P. Sagaut, J.-F. Boussuge, An extended spectral analysis of the lattice boltzmann method: modal interactions and stability issues, J. Comput. Phys. 380 (2019) 311–333.

[28] F. Renard, G. Wissocq, J.-F. Boussuge, P. Sagaut, A linear stability analysis of compressible hybrid lattice boltzmann methods, J. Comput. Phys. 446 (2021) 110649.

[29] G. Wissocq, P. Sagaut, Hydrodynamic limits and numerical errors of isothermal lattice boltzmann schemes, J. Comput. Phys. 450 (2022) 110858.

[30] S. Zhao, G. Farag, P. Boivin, P. Sagaut, Toward fully conservative hybrid lattice boltzmann methods for compressible flows, Phys. Fluids 32 (2020) 126118.

[31] G. Wissocq, T. Coratger, G. Farag, S. Zhao, P. Boivin, P. Sagaut, Restoring the conservativity of characteristic-based segregated models: application to the hybrid lattice boltzmann method, Phys. Fluids 34 (2022) 046102.

[32] K. Bhairapurada, B. Denet, P. Boivin, A lattice-boltzmann study of premixed flames thermo-acoustic instabilities, Combust. Flame 240 (2022) 112049.

[33] G. Searby, Acoustic instability in premixed flames, Combust. Sci. Technol. 81 (1992) 221–231.

[34] G. Searby, D. Rochwerger, A parametric acoustic instability in premixed flames, J. Fluid Mech. 231 (1991) 529–543.

[35] A. Petchenko, V. Bychkov, V. Akkerman, L.-E. Eriksson, Flame–sound interaction in tubes with nonslip walls, Combust. Flame 149 (2007) 418–434.

[36] C. Jiménez, D. Fernández-Galisteo, V. N. Kurdyumov, Flame-acoustics interaction for symmetric and non-symmetric flames propagating in a narrow duct from an open to a closed end, Combust. Flame 225 (2021) 499–512.

[37] W. Meier, P. Weigand, X. R. Duan, R. Giezendanner-Thoben, Detailed characterization of the dynamics of thermoacoustic pulsations in a lean premixed swirl flame, Combust. Flame 150 (2007) 2–26.

[38] P. Weigand, W. Meier, X. Duan, R. Giezendanner-Thoben, U. Meier, Laser diagnostic study of the mechanism of a periodic combustion instability in a gas turbine model combustor, Flow Turbul. Combust. 75 (2005) 275–292.

[39] K. Oberleithner, M. Stöhr, S. H. Im, C. M. Arndt, A. M. Steinberg, Formation and flame-induced suppression of the precessing vortex core in a swirl combustor: experiments and linear stability analysis, Combust. Flame 162 (2015) 3100–3114.

[40] G. Lartigue, U. Meier, C. Berat, Experimental and numerical investigation of self-excited combustion oscillations in a scaled gas turbine combustor, Appl. Therm. Eng. 24 (2004) 1583–1592.

[41] J. Galpin, A. Naudin, L. Vervisch, C. Angelberger, O. Colin, P. Domingo, Large-eddy simulation of a fuel-lean premixed turbu-

lent swirl-burner, Combustion and Flame 155 (2008) 247 – 266. doi:10.1016/j.combustflame.2008.04.004.

[42] B. Fiorina, R. Vicquelin, P. Auzillon, N. Darabiha, O. Gicquel, D. Veynante, A filtered tabulated chemistry model for les of premixed combustion, Combustion and Flame 157 (2010) 465–475.

[43] V. Moureau, P. Domingo, L. Vervisch, From large-eddy simulation to direct numerical simulation of a lean premixed swirl flame: Filtered laminar flame-pdf modeling, Combust. Flame 158 (2011) 1340–1357.

[44] P. Wang, N. Platova, J. Fröhlich, U. Maas, Large eddy simulation of the preccinsta burner, International Journal of Heat and Mass Transfer 70 (2014) 486 – 495. doi:10.1016/j.ijheatmasstransfer.2013.11.025.

[45] D. Veynante, V. Moureau, Analysis of dynamic models for large eddy simulations of turbulent premixed combustion, Combustion and Flame 162 (2015) 4622 – 4642. doi:10.1016/j.combustflame.2015.09.020.

[46] Y. C. See, M. Ihme, Large eddy simulation of a partially-premixed gas turbine model combustor, Proceedings of the Combustion Institute 35 (2015) 1225 – 1234. doi:10.1016/j.proci.2014.08.006.

[47] P. Wang, J. Fröhlich, U. Maas, Z.-x. He, C.-j. Wang, A detailed comparison of two sub-grid scale combustion models via large eddy simulation of the preccinsta gas turbine model combustor, Combust. Flame 164 (2016) 329–345.

[48] P. Bénard, G. Lartigue, V. Moureau, R. Mercier, Large-eddy simulation of the lean-premixed preccinsta burner with wall heat loss, Proc. Combust. Inst. 37 (2019) 5233–5243.

[49] B. Franzelli, E. Riber, L. Y. Gicquel, T. Poinsot, Large eddy simulation of combustion instabilities in a lean partially premixed swirled flame, Combustion and Flame 159 (2012) 621 – 637. doi:10.1016/j.combustflame.2011.08.004.

[50] D. Fredrich, W. P. Jones, A. J. Marquis, Thermo-acoustic instabilities in the preccinsta combustor investigated using a compressible les-pdf approach, Flow Turbul. Combust. 106 (2021) 1399–1415.

[51] P. J. Linstrom, W. Mallard, Nist chemistry webbook; nist standard reference database no. 69 (2001).

[52] B. G. Franzelli, Impact of the chemical description on direct numerical simulations and large eddy simulations of turbulent combustion in industrial aero-engines, Ph.D. thesis, 2011.

[53] S. Blanchard, Q. Cazères, B. Cuenot, Chemical modeling for methane oxy-combustion in liquid rocket engines, Acta Astronaut 190 (2022) 98–111.

[54] A. Vreman, An eddy-viscosity subgrid-scale model for turbulent shear flow: Algebraic theory and applications, Phys. Fluids 16 (2004) 3670–3681.

[55] O. Colin, F. Ducros, D. Veynante, T. Poinsot, A thickened flame model

for large eddy simulations of turbulent premixed combustion, Phys. Fluids 12 (2000) 1843–1863.

[56] B. Rochette, E. Riber, B. Cuenot, O. Vermorel, A generic and self-adapting method for flame detection and thickening in the thickened flame model, Combust. Flame 212 (2020) 448–458.

[57] F. Charlette, C. Meneveau, D. Veynante, A power-law flame wrinkling model for les of premixed turbulent combustion part i: non-dynamic formulation and initial tests, Combust. Flame 131 (2002) 159–180.

[58] F. Charlette, C. Meneveau, D. Veynante, A power-law flame wrinkling model for les of premixed turbulent combustion part ii: dynamic formulation, Combust. Flame 131 (2002) 181–197.

[59] B. Rochette, F. Collin-Bastiani, L. Gicquel, O. Vermorel, D. Veynante, T. Poinsot, Influence of chemical schemes, numerical method and dynamic turbulent combustion modeling on les of premixed turbulent flames, Combust. Flame 191 (2018) 417–430.

[60] S. Taileb, A. Millán-Merino, S. Zhao, P. Boivin, Lattice-boltzmann modeling of lifted hydrogen jet flames: A new model for hazardous ignition prediction, Combust. Flame 245 (2022) 112317.

[61] F. Osmanlic, C. Körner, Lattice Boltzmann method for Oldroyd-B fluids, Computers and Fluids 124 (2016) 190–196.

[62] G. Daviller, G. Oztarlik, T. Poinsot, A generalized non-reflecting inlet boundary condition for steady and forced compressible flows with injection of vortical and acoustic waves, Comput Fluids 190 (2019) 503–513.

[63] T. Poinsot, D. Veynante, Theoretical and numerical combustion, RT Edwards, Inc., 2005.

[64] B. Franzelli, E. Riber, L. Y. Gicquel, T. Poinsot, Large eddy simulation of combustion instabilities in a lean partially premixed swirled flame, Combust. Flame 159 (2012) 621–637.

[65] P. S. Volpiani, T. Schmitt, D. Veynante, Large eddy simulation of a turbulent swirling premixed flame coupling the tfles model with a dynamic wrinkling formulation, Combust. Flame 180 (2017) 124–135.

[66] A. Abdelsamie, G. Lartigue, C. E. Frouzakis, D. Thévenin, The taylor–green vortex as a benchmark for high-fidelity combustion simulations using low-mach solvers, Comput Fluids 223 (2021) 104935.

[67] T. Lu, C. K. Law, A criterion based on computational singular perturbation for the identification of quasi-steady state species: A reduced mechanism for methane oxidation with no chemistry, Combustion and Flame 154 (2008) 761–774. doi:https://doi.org/10.1016/j.combustflame.2008.04.025.

Appendix A. TFLES filtered equations

Large-eddy simulations are performed over the filtered form of the NS equations (1),

$$\frac{\partial \overline{\rho}}{\partial t} + \frac{\partial \overline{\rho}\tilde{u}_\beta}{\partial x_\beta} = 0 \tag{A.1a}$$

$$\frac{\partial \overline{\rho}\tilde{u}_\alpha}{\partial t} + \frac{\partial \overline{\rho}\tilde{u}_\alpha\tilde{u}_\beta}{\partial x_\beta} = -\frac{\partial \hat{p}}{\partial x_\alpha} + \frac{\partial \check{\tau}_{\alpha\beta}}{\partial x_\beta} \tag{A.1b}$$

$$\frac{\partial \overline{\rho}\tilde{E}}{\partial t} + \frac{\partial \overline{\rho}\tilde{H}\tilde{u}_\beta}{\partial x_\beta} = \frac{\partial \check{\tau}_{\alpha\beta}\tilde{u}_\alpha}{\partial x_\beta} - \frac{\partial \check{q}_\beta}{\partial x_\beta} \tag{A.1c}$$

$$\frac{\partial \overline{\rho}\tilde{Y}_k}{\partial t} + \frac{\partial \overline{\rho}\tilde{u}_\beta\tilde{Y}_k}{\partial x_\beta} = \frac{\partial \check{J}^k_\beta}{\partial x_\beta} + \check{\dot{\omega}}_k \tag{A.1d}$$

in which $\bar{\cdot}$ denotes the filtered values, $\tilde{\cdot}$ the Favre filtered quantities, $\hat{\cdot}$ the resolved variables and $\check{\cdot}$ the modeled terms. The turbulent viscous tensor is modeled as

$$\check{\tau}_{\alpha\beta} \equiv (\hat{\mu} + \mu_t)\left(\frac{\partial \tilde{u}_\alpha}{\partial x_\beta} + \frac{\partial \tilde{u}_\beta}{\partial x_\alpha} - \delta_{\alpha\beta}\frac{2}{3}\frac{\partial \tilde{u}_\gamma}{\partial x_\gamma}\right) . \tag{A.2}$$

with μ_t the sub-grid turbulence viscosity, which is calculated using the Vreman model [17, 54] in the current study.

The classical thickened-flame framework [55, 57–59] is chosen to simulate the turbulent premixed flame. The heat transfer, species diffusion, and chemistry source terms in the above equations are evaluated as

$$\check{q}_\alpha = -\left[\mathcal{S}\mathcal{F}\Xi\hat{\lambda} + (1-\mathcal{S})(\lambda+\lambda_t)\right]\frac{\partial \hat{T}}{\partial x_\alpha} + \sum_{k=1}^{\mathrm{N_{sp}}}\hat{h}_k\check{J}^k_\alpha \tag{A.3a}$$

$$\check{J}^k_\alpha = \left[\mathcal{S}\mathcal{F}\Xi + (1-\mathcal{S})\left(1+\frac{\mathcal{D}_{k,t}}{\mathcal{D}_k}\right)\right]\hat{J}^k_\alpha \tag{A.3b}$$

$$\check{\dot{\omega}}_k = \mathcal{S}\frac{\Xi}{\mathcal{F}}\hat{\dot{\omega}}_k \tag{A.3c}$$

The factor $\mathcal{S}$ is a flame sensor whose value is one inside the flame and zero otherwise. So, outside the flame (i.e. $\mathcal{S} = 0$), this method simply adds the sub-grid heat and species diffusion using turbulence conductivity and diffusivity,

$$\lambda_t = \frac{\mu_t \hat{c_p}}{\mathrm{Pr_t}} \ , \ \mathcal{D}_{k,t} = \frac{\mu_t}{\overline{\rho}\mathrm{Sc_t}} \ , \tag{A.4}$$

where $\mathrm{Sc_t}$ and $\mathrm{Pr_t}$ are the turbulent Schmidt and Prandtl numbers respectively. Inside the flame region ($\mathcal{S} = 1$), the flame thickness is artificially enlarged by $\mathcal{F}$ times to be well resolved by the mesh grid, and the sub-grid wrinkling factor Ξ is considered to compensate the turbulent flame speed lost due to the thickening of the flame. It is evaluated following a dynamic procedure introduced in [59], i.e.

$$\Xi = \left(\frac{\Delta}{\delta_L^0}\right)^{\beta} \tag{A.5}$$

with Δ the LES filter size, usually taken around the thickened flame thickness and δ_L^0 the laminar flame thickness. The exponent β is set to 0.5 in this study.

Appendix B. The pseudo-DDF spatial derivative method

The pseudo-DDF method for total energy flux has just been developed recently inspired by the DDF method, which is quite widely used in the LBM community, and the conservative schemes for scalar transport in hybrid LB methods [30]. It is evaluated from a constructed population on neighbor lattices

$$\nabla \cdot (\overline{\rho}\tilde{\boldsymbol{u}}\tilde{H}) = \frac{1}{\Delta t}\sum_{i=1}^{19}\left[f_i^H(\boldsymbol{x},t) - f_i^H(\boldsymbol{x} - \boldsymbol{c_i}\Delta t, t)\right] \tag{B.1}$$

where $\boldsymbol{c_i}$ is the discrete velocities of the i-th lattice, and f_i^H is constructed from the collide population of the flow fields f_i (detailed expression of this

population can be found in [13]) as

$$f_i^H(\boldsymbol{x},t) \equiv \tilde{H}(\boldsymbol{x},t) f_i(\boldsymbol{x},t) + f_i^{H,\mathrm{neq}}(\boldsymbol{x},t). \tag{B.2}$$

The off-equilibrium counterpart $f_i^{H,\mathrm{neq}}$ is obtained from its first-order Hermite coefficient as

$$f_i^{H,\mathrm{neq}}(\boldsymbol{x},t) = \omega_i \left(\sum_{\alpha=1}^{3} \frac{c_{i\alpha} a_\alpha^{H,\mathrm{neq}}(\boldsymbol{x}, t-\Delta t)}{c_s^2} \right) \tag{B.3}$$

where ω_i is the weight of the lattice i and the Hermite coefficients are constructed as

$$a_\alpha^{H,\mathrm{neq}}(\boldsymbol{x},t) = \frac{\Delta t}{2} \left((\overline{\rho}\tilde{u}_\alpha \tilde{H})(\boldsymbol{x},t) - c_{i\alpha}(f_i^{\tilde{H}})(\boldsymbol{x} - \boldsymbol{c_i}\Delta t, t) \right) \tag{B.4}$$

This new numerical scheme mimics a Double Distribution Function (DDF) method using only three new degrees of freedom ($a_\alpha^{H,\mathrm{neq}}$) for one scalar instead of 19. It yields excellent stability as well as second-order space/time accuracy. Figure B.10 reports the order of convergence of such a scheme measured by a one-dimensional passive scalar transport test. The relative error obtained from different numbers of grid points confirms that the designed scheme achieves second-order accuracy.

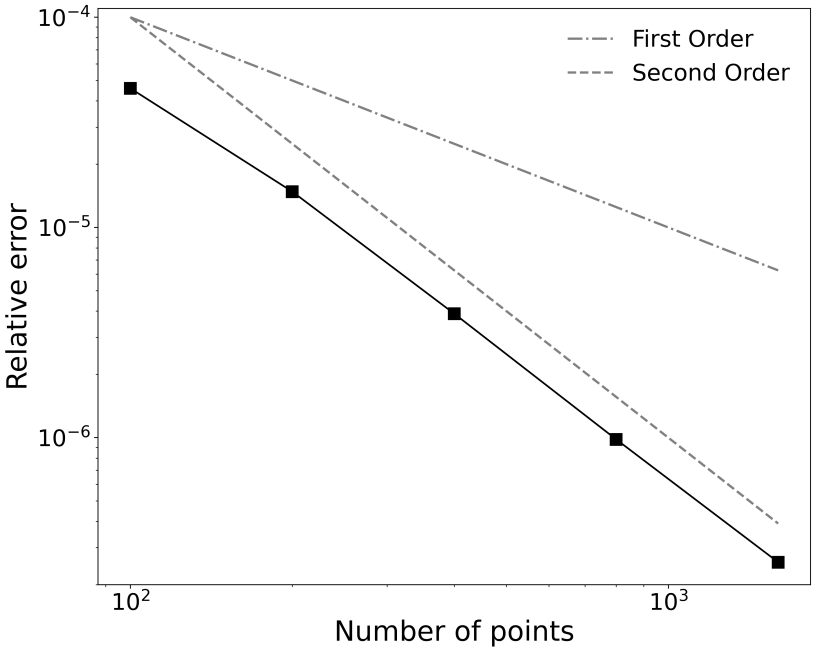

Figure B.10: Convergence order of the pseudo-DDF method.